Proceedings of ASME Turbo Expo 2025
Turbomachinery Technical Conference and Exposition
GT2025
June 16-20, 2025, Memphis, Tennessee

GT2025-152640

REYNOLDS NUMBER EFFECT ON TRANSITIONAL DELAYED DETACHED-EDDY SIMULATION

Felix M. Möller[1,*], Michael Bergmann[2], Christian Morsbach[2], Paul G. Tucker[3], Zhong-Nan Wang[4], Alexander Hergt[2], Florian Herbst[2]

[1]Institute of Test and Simulation for Gas Turbines, German Aerospace Center (DLR), Cologne, Germany
[2]Institute of Propulsion Technology, German Aerospace Center (DLR), Cologne, Germany
[3]Department of Engineering, University of Cambridge, Cambridge, United Kingdom
[4]College of Engineering and Physical Sciences, University of Birmingham, Birmingham, United Kingdom

ABSTRACT

The accurate prediction of a wide range of operating conditions is desired by numerical methods. In particular, off-design conditions are a major challenge for steady Reynolds-averaged Navier-Stokes (RANS) methods. In this study, we evaluate the delayed detached-eddy simulation (DDES) method for these flow conditions. Therefore, we consider a transitional linear compressor cascade, which has been measured experimentally at DLR for different Reynolds numbers and inflow angles. For the lowest Reynolds number, numerical large-eddy simulation (LES) reference data is available additionally. We begin with a basis validation for Re = 150 000 at the aerodynamic design point before evaluating off-design conditions, characterized by positive and negative incidence angles, for this Reynolds number. This is followed by a Reynolds number variation up to Re = 900 000 for two off-design inflow angles. The potential for the transitional DDES is visible for the lowest Reynolds number where reference data is met well with a noticeable reduction of computational resources. The Reynolds number variation yield two-fold results. While the negative incidence confirmed the beneficial behavior of DDES, the positive incidence reveals deficits of the DDES for this specific setup. We give explanations for the improved, but also the limited behavior and discuss the mesh requirements, directly linked the computational requirements.

Keywords: Turbulence modeling, hybrid RANS/LES, Delayed Detached-Eddy Simulation, compressor cascade, Reynolds number, transition, wake losses

NOMENCLATURE

Roman letters

c	Chord length [m]
c_{ax}	Axial chord length [m]
C_f	Skin friction coefficient [-]
D_k	Destruction term of modeled k [kg m^{-1} s^{-3}]
f_d	Spalart's shielding function [-]
k	Turbulent kinetic energy [m^2 s^{-2}]
l	Length scale [m]
M_{is}	Isentropic Mach number [-]
N	Number of cells [-]
p_s	Static pressure [Pa]
p_t	Total pressure [Pa]
Re	Reynolds number [-]
t_c	Convective time [-]
u, v, w	Velocity components [m s^{-1}]
x, y, z	Cartesian coordinates [m]

Greek letters

β_1	Inflow angle [°]
γ	Intermittency [-]
Δ_{SLS}	Sub-grid length scale [m]
$\Delta x^+, \Delta y^+, \Delta z^+$	Non-dimensional cell sizes [-]
η	Wall-normal coordinate [m]
κ	Specific heat capacity ratio [-]
ν	Kinematic viscosity [m^2 m^{-1}]
ρ	Density [kg m^{-3}]
σ_b	Blending factor [-]
τ_w	Wall shear stress [Pa]
ω	Total pressure loss coefficient [-]

Subscripts

int	Area-integrated quantity
mag	Magnitude value
mod	Modeled component
rel	Relative quantity
res	Resolved component
tang	Tangential component
1,2	Quantities at measurement plane 1 or 2
SS,PS	Suction or pressure side
i, j	Streamwise or wall-normal index

*Corresponding author: felix.moeller@dlr.de

1. INTRODUCTION

Powerful numerical methods in the modern turbomachinery design process are key to tackle recent challenges of the aerospace industry. Design improvements and, thus, increased engine efficiencies require the reliable computational prediction of actual flow physics. The entire operating range of a jet engine can be characterized by the Reynolds number, Mach number and inflow angle variation. While the Reynolds number is influenced by the flight altitude, the inflow angle changes when the operating point of an engine is changed at a constant altitude. Predicting this wide range of operating conditions reliably with computational fluid dynamics (CFD) methods is an important aspect in the numerical turbomachinery design process and still faces a big challenge, especially for current state-of-the-art methods such as steady Reynolds-averaged Navier-Stokes (RANS) [1–3]. To be more precise, RANS methods have been developed and improved over the last decades and are now well-established for predicting moderate flow conditions at the aerodynamic design point (ADP), i.e. attached boundary layers, with satisfactory accuracy. In off-design conditions, characterized by massive separation and high unsteadiness, RANS simulations are not able to treat these phenomena accurately enough.

At this point, the logical evolutionary computational approach would be large-eddy simulation (LES). This method has proven its potential and capabilities for turbomachinery applications in the recent past [4–7]. While the physical accuracy is indisputable, this method comes at a price - the computational effort is significantly higher compared to steady RANS models. Since the required mesh points, especially in wall-vicinity, scale with the Reynolds number [8], LES is preferably used in the low Reynolds number regimes as also illustrated by Bergmann et al. [9].

As a popular compromise between fast computational results and high physical accuracy, hybrid RANS/LES (HRL) methods are gaining more attention. The number of hybrid concepts is increasing and the seamless HRL method, namely delayed detached-eddy simulation (DDES), is a promising approach to increase the predictive accuracy in complex turbomachinery application at affordable computational resources. As stated by the model name, this method has been proposed for detached flows. In these regions, LES-behavior is aimed. On the other side, in the attached boundary layer and closest wall-vicinity, this model stays in RANS-mode. Therefore, a coarser mesh resolution can be used in this region, which explains the reduced computational requirements compared to pure LES.

The effect of varying Reynolds numbers on separation behavior and laminar-to-turbulent transition is well understood experimentally and also investigated with RANS approaches [10, 11], but to the author's knowledge, studies of these effects with DDES are rare. Most of the investigations with Reynolds number variation have been carried out for the circular cylinder test case as also done by Mays et al. [12]. Zhou et al. [13] have introduced a transitional DDES model and also investigated turbomachinery components, but other than that, the literature research yield a small number of references focusing on a wide range of operating conditions within a single study. Typically, DDES studies are conducted for a single operating point by fixed flow conditions, which motivates our work. Within this study, an assessment of the DDES method for various Reynolds numbers and inflow angles will be discussed. We aim to work out differences to steady RANS results, illustrate improvements but also limitations and development potential.

In addition to that, the mesh requirements for specific flow conditions (i.e. transitional, separated boundary layer) for DDES methods have not been well-analyzed yet. Typically, the mesh is characterized by the non-dimensional cell sizes $\Delta x^+, \Delta y^+, \Delta z^+$. Tucker [14] (p. 114, Tab. 3.4) recommended best-practice ranges for different simulation approaches, mainly based on attached, fully turbulent flows. Therefore, we will re-evaluate if these values are still applicable to transitional, separated flows in the present study. These aspects lead to the following research questions to be answered by this study:

- How does DDES perform in predicting a wide range of operating conditions for a transitional compressor cascade?
- How meaningful are the non-dimensional cell sizes as mesh criteria for the transitional DDES?

2. METHODOLOGY

2.1 Transitional Delayed Detached-Eddy Simulation

This work focuses on the hybrid RANS/LES method DDES in its version of Spalart et al. [15]. This model is based on the SST turbulence model by Menter [16]. To 'hybridize' the classical RANS turbulence model, the denominator of the modeled turbulent kinetic energy (TKE) destruction term is changed as follows:

$$\mathrm{D}_{k_{\mathrm{mod,RANS}}} = \frac{\rho k_{\mathrm{mod}}^{3/2}}{l_{\mathrm{RANS}}} \Rightarrow \mathrm{D}_{k_{\mathrm{mod,DDES}}} = \frac{\rho k_{\mathrm{mod}}^{3/2}}{l_{\mathrm{DDES}}} \tag{1}$$

where ρ, k_{mod} and l_{RANS} or l_{DDES} represent the density, modeled turbulent kinetic energy and specific length scale respectively. The newly introduced DDES length scale l_{DDES} compares the RANS length scale and a computed sub-grid length scale (SLS) with the following expression:

$$l_{\mathrm{DDES}} = l_{\mathrm{RANS}} - f_d \max\left(0, l_{\mathrm{RANS}} - C_{\mathrm{DDES}}\Delta_{\mathrm{SLS}}\right) \tag{2}$$

where f_d is the shielding function proposed by [15], $C_{\mathrm{DDES}} = 0.65$ and Δ_{SLS} is the respective SLS approach. Originally, this parameter was determined based on grid-specific values only [17], making this variable very sensitive to the mesh quality. Vorticity-based SLS approaches have been proposed in the past that aim to reduce the impact of the mesh quality and incorporate also physical information such as the vorticity, especially in developing shear layers. An assessment of different SLS approaches has been made beforehand, but will not be addressed in this paper. We apply the vorticity-based SLS approach of Shur et al. [18], which was found to yield best results.

The original DDES method was proposed and developed for fully turbulent flows. The flow through the compressor cascade, considered in this work, is characterized by laminar-to-turbulent transition which emphasizes the need to account for transition numerically. Recently, we introduced a transitional DDES method [19, 20] and discussed the predictive quality for

separation-induced and bypass transition. The transitional DDES is coupled with the one-equation γ-transition model of Menter et al. [21] by neglecting the additional production term P_k^{lim}, introduced for steady RANS simulations. Detailed discussions on this model modification can be found in [19, 20].

2.2 Numerical solver

All simulations have been carried out with the DLR turbomachinery in-house solver TRACE[1] developed and validated at the Institute of Propulsion Technology in the Department for Numerical Methods [22] in close collaboration with MTU Aero Engines. Conducted steady RANS and DDES simulations employ the density-based finite-volume branch of this solver, with a spatial discretization of 2$^{\text{nd}}$-order accuracy. For all unsteady simulations, the 3$^{\text{rd}}$-order explicit Runge-Kutta method [23] was used. The physical time step for these simulations was defined to meet CFL ≤ 1.

To account for resolved turbulence in the separated regions, Travin et al. [24] proposed a dynamic Riemann solver blending. The fully upwind scheme (in its formulation of Roe [25]) was found to be too dissipative to resolve turbulence accurately [26]. Therefore, this method determines a blending factor σ_{b} between zero (fully central $\rightarrow$ desired in resolved parts of the domain) and unity (fully upwind $\rightarrow$ desired in modeled regions, hence, attached boundary layers). Nevertheless, $\sigma_{\text{b}} = 0$ (fully central) can cause stability issues and undesired numerical oscillations, which is why we defined a lower limit of the blending factor to ensure at least 5 % damping upwind flux

$$\sigma_{\text{b,limit}} = \max\left(0.05, \sigma_{\text{b,original}}\right). \tag{3}$$

Finally, all simulations were performed with the stagnation point anomaly fix by Kato and Launder [27] to avoid unphysical overproduction of turbulent kinetic energy at the blade leading edge.

2.3 Assessment approach

To tackle the aforementioned research questions within this study, we compare

- Experimental reference data,
- Numerical LES reference data (where available),
- Transitional RANS,
- Transitional DDES

with a specific focus on the DDES results. The beneficial performance of a transitional DDES has been thoroughly investigated in [20] which is why we omit showing results of the baseline DDES without a transition model in this work. The RANS model uses exactly the same transition model as the DDES, thus ensuring the best possible comparability of numerical results.

While we primarily focus on the predictive quality of DDES for changing operating conditions (varying Reynolds number and inflow angle), we also analyze the results at different mesh densities to work out the requirements for changing operating conditions.

[1] https://www.trace-portal.de/userguide/

3. TEST CASE

3.1 Experimental setup

The DLR-LRN (low Reynolds number) compressor cascade was designed and experimentally measured at the Institute of Propulsion Technology by Hergt et al. [28]. Key aerodynamic design parameters are summarized in Tab. 1 and served as a basis for the numerical setup. The experiments have been conducted

TABLE 1: Aerodynamic design parameters of the DLR-LRN compressor cascade.

Parameter	Value
Pitch l_{pitch}	$= 4.039 \times 10^{-2}$ m
Chord c	$= 7 \times 10^{-2}$ m
Axial chord c_{ax}	$= 6.725 \times 10^{-2}$ m
Stagger angle β_{s}	$= 16.04°$
Inlet Reynolds number Re_1	$= 1.5 \times 10^5$
Inlet Mach number $\text{M}_{\text{is},1}$	$= 0.6$
Inflow angle β_1 (at ADP)	$= 133°$
AVDR (at ADP)	≈ 1.03
Inflow FSTI	≈ 0.5 %

for four different Reynolds numbers ($\text{Re}_1 = 1.5 \times 10^5$, 2.5×10^5, 3.5×10^5 and 9.0×10^5). In addition, five inflow angles ($\beta_1 = 133°$, +/-2° and +/-5°) were measured for each Reynolds number which yields a comprehensive measurement matrix. The notation of the inflow angle is illustrated in Fig. 1. This will

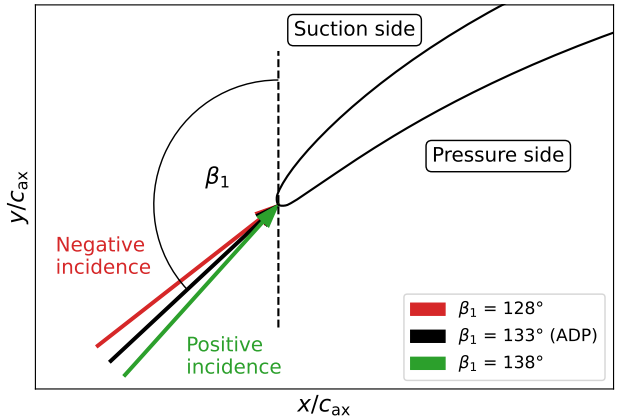

FIGURE 1: Definition of the inflow angle and illustration of positive/negative incidence.

help as an orientation for later discussions about positive/negative incidence. For each operating point, the following experimental reference data is available:

- Measured inlet and outlet boundary condition (BC)
- Static pressure measurements along the blade surface
- Pitchwise measurements in the wake region (downstream of the trailing edge)

3.2 Numerical representation

An illustration of the computational domain is shown in Fig. 2 with an inlet and outlet panel position at $x/c_{\text{ax}} = -0.89$

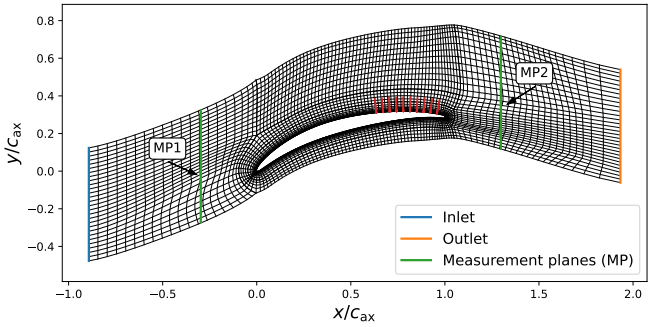

FIGURE 2: Illustration of the numerical domain with a blade-to-blade view in the *x*-*y*-plane. The mesh is shown for the coarsest setup as an example.

and $x/c_{ax} = 1.93$, respectively. In addition, the two pitchwise measurement planes (MP) are shown as well as an exemplary x-y-plane mesh resolution (illustrated for $Re_1 = 1.5 \times 10^5$ and the coarsest version). Details about the meshes will be discussed in the following sections. In pitchwise direction, a periodic BC is applied for all simulation types. In spanwise direction, we differ between steady RANS and DDES simulations where we use inviscid walls and a periodic BC respectively. The span extent for RANS and DDES setups is $0.03c_{ax}$ and $0.2c_{ax}$ respectively. The span extent for DDES was dictated by the numerical LES reference [9]. To guarantee best comparability, we have applied the identical span size. Inflow and outflow BC are defined by the experiments. At the inlet, the total pressure p_t, total temperature T_t and inflow angle β_1 are prescribed and differ for each operating point. Turbulent quantities such as free-stream turbulence intensity (FSTI) and the turbulent length scale l_{RANS} were kept constant for all simulations. A verification of comparable turbulent states between simulations and the experiment is done by comparing the pitchwise area-integrated turbulence intensity at MP1. The outlet is defined by a constant back pressure BC which is also extracted from experimental data. To account for the axial velocity-density ratio (AVDR), all numerical simulations used an additional source term implemented in the version of Giles [29] and Bolinches et al. [30]. With this term, the effects of the streamline contraction in the experiment are mimicked.

To ensure well-converged statistics for the DDES simulations, we ran all simulations for 40 effective through flows after removing the initial transient which was detected by the method introduced by Bergmann et al. [31]. The statistical error calculated for the variables considered below is at the level of the line width and is therefore not shown in the following. The time for a physical through flow in our case is defined by $t_c = c/u_{mag,1,int}$ with the blade chord length c and the pitchwise area-integrated velocity magnitude at MP1.

4. BASIS VALIDATION FOR RE = 150 000

Before assessing the transitional DDES for varying Reynolds numbers, we focus on the lowest one. Bergmann et al. [9] have conducted a comprehensive LES study for this Reynolds number which serves as a validated high-fidelity reference. Based on this data, in combination with the experimental reference, the DDES method can be best evaluated.

4.1 Meshing strategy

We designed a baseline mesh based on best practice meshing guidelines for HRL meshes (e.g. [14]). Starting from there, we halved and doubled the number of cells in each direction yielding a global 2^3 coarsening/refinement. A summary of the generated meshes for $Re_1 = 1.5 \times 10^5$ can be found in Tab. 2. The interested

TABLE 2: Created mesh setups for Re = 150 000.

	N_{total}	N_{2D}	N_z
Coarse (halved)	66 075	4 405	15
Intermediate (baseline)	528 600	17 620	30
Fine (doubled)	4 228 800	70 480	60

reader can look up further mesh properties in Appendix A. This also applies to the resulting non-dimensional cell sizes, which we omit showing here. As mentioned above, these numbers do not seem to provide a meaningful orientation for separated and transitional cases. The generated meshes for this Reynolds number range from a very coarse to a sensibly fine resolution, in terms of total number of cells, but the non-dimensional cell sizes appear to be very small. Results on these three meshes will be discussed in the following. All presented RANS results in this study are based on the fine resolution (guaranteeing a Grid Convergence Index [32] $GCI^{21}_{fine} \leq 2.2\,\%$). Since the steady RANS simulations are conducted as 2D simulations, N_{2D} in Tab. 2 is the relevant number of total cell counts in this case.

4.2 Aerodynamic design point

We start with the single operating point at the ADP, characterized by $Re_1 = 1.5 \times 10^5$ and $\beta_1 = 133°$. In addition to the above-mentioned reference data, [9] also investigated LES without a synthetic turbulence generator (STG) (meaning zero inflow turbulence) for this specific conditions. We additionally show these results in the following to better evaluate the DDES simulations.

Initially, we discuss the isentropic Mach number M_{is} in Fig. 3 which is defined as

$$M_{is}(x_{rel}) = \sqrt{\frac{2}{\kappa - 1}\left(\frac{p_{t,1,int}}{p_s(x_{rel})}^{\frac{\kappa-1}{\kappa}} - 1\right)} \tag{4}$$

where $p_{t,1,int}$ is the pitchwise area-integrated total pressure at MP1, p_s is the static pressure along the blade surface and $\kappa = 1.4$ is the specific heat capacity ratio. The relative x-coordinate in blade chord direction is defined as

$$x_{rel} = \left[\sqrt{x^2 + y^2} \cdot \cos\left(\arctan\left(\frac{y}{x}\right) - \beta_s\right)\right] / c \tag{5}$$

with the blade chord length c and stagger angle β_s, where $x_{rel} = 0$ is at the leading edge and unity at the trailing edge. Both parameters are introduced in Tab. 1. For LES to match the experiment, it is important to incorporate even the small amount of resolved FSTI ($\approx 0.4\,\%$ at MP1) with an STG, as discussed in [9]. In Fig. 3, it can be seen that the LES without STG shows a different pressure distribution along the blade surface. Turning to the RANS result, one might think that it agrees quite well with the experimental data. At this point, the validated high-fidelity

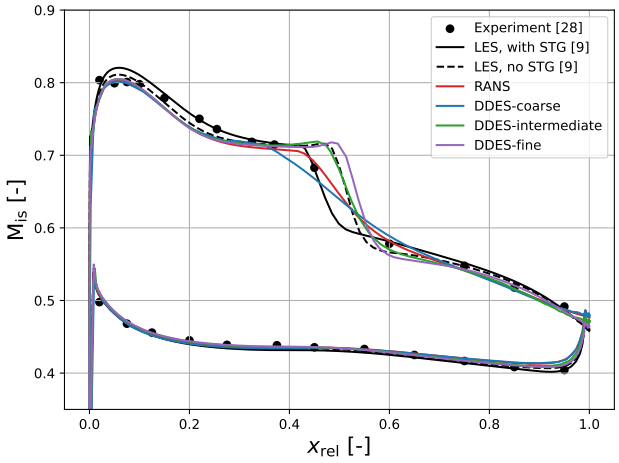

FIGURE 3: Isentropic Mach number along the blade surface at the aerodynamic design point for Re = 150 000.

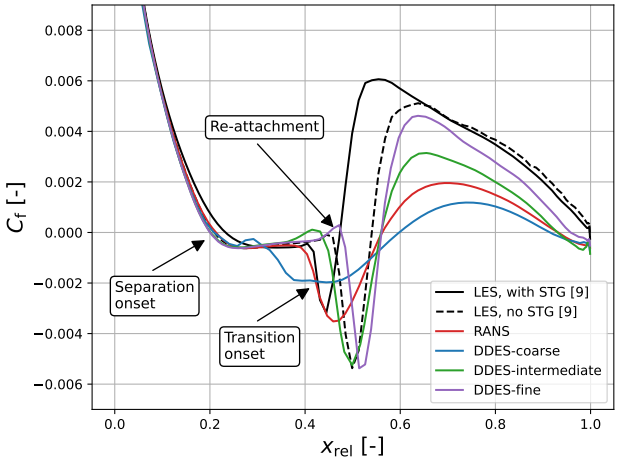

FIGURE 4: Skin friction coefficient along the blade suction side at the aerodynamic design point for Re = 150 000. Relevant events are marked for LES with STG as an example.

LES reference reveals, that the separation bubble is predicted wrong by RANS. Due to missing measurement locations inside the separation bubble, this cannot be derived from experimental data. The three DDES results on different meshes show different trends. DDES-coarse mainly follows the RANS results with an even worse agreement with the experiment. The two finer simulations DDES-intermediate and DDES-fine do show a more pronounced separation bubble compared to the experiment and also LES with STG. For consistency reasons, all DDES simulations are conducted without an STG, because at least the coarsest setups cannot sustain the incoming resolved turbulence. DDES-intermediate shows almost identical results to the LES simulation without the STG. This highlights the capabilities of DDES for the transitional case at this point. The even finer simulation, DDES-fine, shows a slightly different separation bubble shape ending in the same re-attachment location as DDES-intermediate. All in all, the blade pressure distribution is met well with the intermediate and fine DDES.

To better understand the mechanisms of the separation-induced transition on the blade suction side, we show the skin friction coefficient C_f in Fig. 4. This non-dimensional wall shear stress is defined by

$$C_f(x_{rel}) = \mathrm{sgn}\left(\tau_{w,x}(x_{rel})\right) \frac{\tau_{w,mag}(x_{rel})}{0.5\rho_{1,int}\, u^2_{mag,1,int}} \qquad (6)$$

with the sign of the wall shear stress x-component $\tau_{w,x}$ and the norm of the wall shear stress vector $\tau_{w,mag}$ along the blade surface. $\rho_{1,int}$ is the pitchwise area-integrated density at MP1. For C_f, no experimental data is available. All simulations without STG show a slightly earlier separation than the LES with STG, because the secondary instability of resolved free-stream disturbances is not taken into account. This is also seen in Fig. 3 by reduced M_{is} values between $0 < x_{rel} \leq 0.2$. The boundary layer develops differently until the separation which can be explained by the missing resolved turbulence. In Sec. 3.2 we have introduced, that the FSTI was ensured to be comparable to experimental and LES (with STG) data. Since we are running all simulations without STG, the FSTI level prescribed at the inlet, and met at MP1, corresponds to modeled FSTI. What we learn from Fig. 4, is, that the modeled inlet turbulence has no physical effect on capturing the separation and transition process accurately. This is also confirmed by the LES results without STG, because the separation bubble is also predicted differently from the one with STG. Nevertheless, all DDES simulations and the RANS simulation agree well with the LES without STG until the separation onset. From there on, the simulations develop differently. RANS shows good agreement with the LES reference with STG until the transition onset ($x_{rel} \approx 0.4$), but the separation bubble size is over-predicted. The coarse DDES setup shows worse results with a premature transition process and the largest separation bubble size. DDES-intermediate captures the transition process qualitatively better, but the transition onset location is further downstream ($x_{rel} \approx 0.45$) and the DDES converges towards the LES results without STG. An even finer resolution yields a delayed transition onset, but an improved recovery of the boundary layer after reattachment can be seen, where DDES-fine gets much closer to the LES reference. The trend for the finest mesh can be explained by the, potentially, 'too fine' resolution yielding in a reduction of modeled TKE to almost zero. Whilst no resolved turbulence is provided, the turbulent content can only be produced by instabilities in the separated shear layer and by the underlying RANS sub-grid model. If the latter is reduced to zero, we obtain a delayed transition. A detailed discussion about the interaction of modeled and resolved TKE for separation-induced transition can be found in [19]. The improved state of the boundary layer after the re-attachment demonstrates, that the DDES-fine generally behaves like an LES with missing turbulent content upstream. The tendency of a secondary separation bubble at $0.45 \leq x_{rel} \leq 0.5$, as seen in DDES-intermediate, DDES-fine and the LES without STG, can also be explained by the missing resolved turbulent content.

To assess how the mesh density affects the predictive quality in the wake region, we plot the total pressure loss coefficient ω

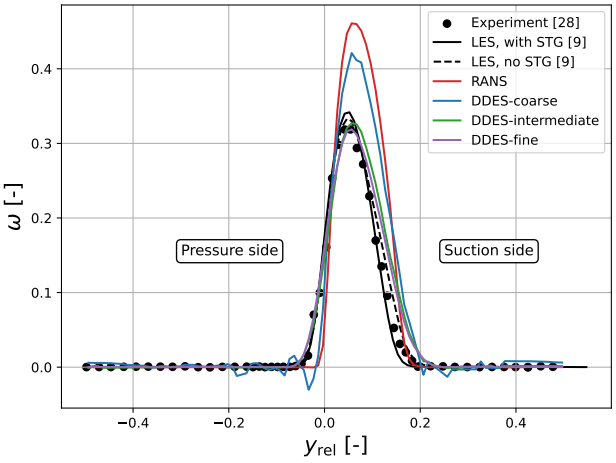

FIGURE 5: Total pressure loss coefficient at MP2 (see Fig. 2) and the aerodynamic design point for Re = 150 000.

in Fig. 5 which is defined by

$$\omega(y_{rel}) = \frac{p_{t,1,int} - p_{t,2}(y_{rel})}{p_{t,1,int} - p_{s,1,int}}. \quad (7)$$

Again, $p_{t,1,int}$ and $p_{s,1,int}$ are the pitchwise area-integrated total and static pressure, respectively, at MP1, while $p_{t,2}$ is the total pressure at MP2. The relative pitchwise coordinate is defined by $y_{rel} = y/l_{pitch}$, where $y_{rel} = 0$ is at the blade trailing edge. Trends from previous results are also seen in Fig. 5, RANS and DDES-coarse overpredict the maximum total pressure loss. Additionally, oscillations by the DDES-coarse are visible in the free-stream which emphasize that the mesh setup is too coarse to conduct a sensible unsteady simulation. With refined meshes, DDES converges towards LES and experiment. The peak value is matched perfectly, while small deviations can be seen on the suction side of the loss curve. DDES-intermediate and DDES-fine slightly overpredict the separation bubble size on the blade surface which yields a slightly wider wake. The convergence of finer DDES meshes towards the LES without STG is also seen here.

The refined DDES results show a good agreement with the reference data and DDES can improve the prediction of both the separation-induced transition and the wake flow compared to RANS. Differences to the LES reference could be explained by a comparison with an LES simulation without STG. At the same time, the coarsest DDES setup did not yield improvements. Having discussed the impact of the STG on the transition process, we omit showing LES reference data without STG in the following.

4.3 Incidence variation

After our analysis of the ADP, we now extend the assessment towards the borders of the operating range. RANS typically fails to predict these off-design conditions and within this sub-section, we work out the capabilities of DDES on the same three mesh versions introduced in Sec. 4.1. To assess the polar at a constant Reynolds number, we varied the inflow angle and consider $\beta_1 = 128°$, $\beta_1 = 133°$, $\beta_1 = 138°$, also illustrated in Fig. 1. The two additional inflow angles ($\beta_1 = 128°$ and $\beta_1 = 138°$) represent off-design operating points for the investigated compressor cascade.

The effect of varying incidence can be seen in the skin friction coefficient in Fig. 6. This time, we show C_f on the blade suction and the pressure side. Focusing the pressure side (dashed lines), numerical results for $\beta_1 = 133°$ and $\beta_1 = 138°$ almost collapse. This changes with the negative incidence ($\beta_1 = 128°$). The LES reference illustrates, that a small leading edge separation occurs on the blade pressure side (see 6-①) with a rapid re-attachment and turbulent boundary layer downstream. This leading edge separation cannot be captured correctly by RANS resulting in an oscillating C_f trend close to leading edge. The development of the turbulent boundary layer is delayed too. The previously seen convergence of different DDES mesh resolutions can also be observed here. DDES-coarse is not capable of capturing the pressure side flow accurately and shows an even larger discrepancy than RANS. The refined meshes show better agreement with LES while the finest is also closest.

Focusing the blade suction side (solid lines) for both off-design inflow angles we see the effect of the incidence angle on the separation and reattachment locations. Basically, with increasing inflow angle, the separation bubble shifts upstream towards the blade leading edge and shrinks. For $\beta_1 = 128°$, RANS and DDES-coarse show deviations from LES in the separated region, but, interestingly, the reattachment point is closer to LES (see 6-②). The opposite trend is seen for DDES-intermediate, which shows an identical transition onset ($x_{rel} \approx 0.6$) but an over-prediction of the separation bubble size in relation to LES. This becomes even more pronounced with DDES-fine. The missing free-stream turbulence, as discussed in Sec. 4.2, plays also an important role for the closure of the separation bubble. Missing instabilities in the separated shear layer yield an over-prediction of the separation bubble size. After the re-attachment, the finer DDES does converge towards LES, describing the turbulent boundary layer more accurately (see 6-③). The results for the positive incidence ($\beta_1 = 138°$) show another trend. Here, we see a closer agreement of DDES-intermediate and DDES-fine with LES reference data for both, the transition onset but also the re-attachment location (see 6-④ and -⑤ respectively). RANS and DDES-coarse are showing almost identical trends with a massive over-prediction of the separation bubble size (see 6-⑥). The different trends for the DDES fit well in the discussion of missing resolved turbulence. The separation-induced transition for this case relies on a very low level of FSTI. In case of a longer separation bubble ($\beta_1 = 128°$), growing instabilities in the separated shear layer support the prediction of separation-induced transition by DDES. Once the separation bubble becomes shorter ($\beta_1 = 133° \rightarrow \beta_1 = 138°$), the transition onset is delayed.

A link between the separation bubble size, the boundary layer state close to the trailing edge and the wake losses can be made with Fig. 7. We show the total pressure loss coefficient ω for all three inflow angles. Overall, RANS over-predicts the loss for all operating points. For the negative incidence ($\beta_1 = 128°$), the well-resolved unsteady simulations agree well. DDES-coarse shows deviations and spurious oscillations (see 7-①). Capturing the leading edge separation on the blade pressure side (see 6-①) has a positive effect on the left-hand flank of the wake loss curve while DDES converges towards LES (see 7-②). The maximum peak value does not appear to be affected by the

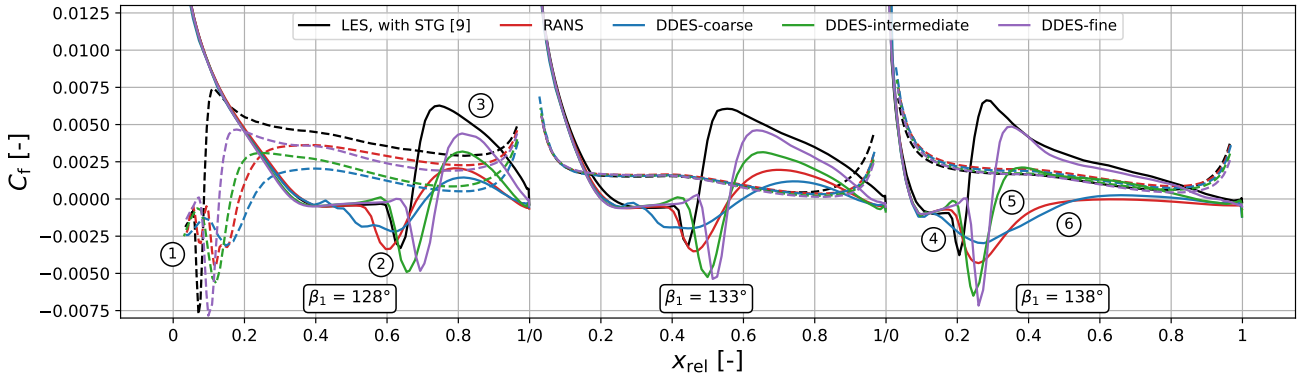

FIGURE 6: Skin friction coefficient along the blade suction (—) and pressure (- -) side for varying inflow angles for Re = 150 000.

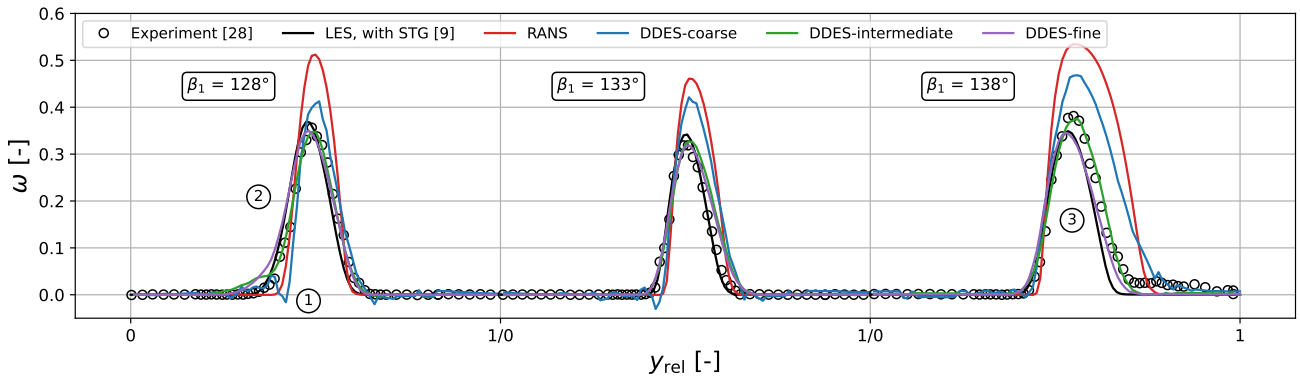

FIGURE 7: Total pressure loss coefficient at MP2 (see Fig. 2) for varying inflow angles for Re = 150 000.

pressure side boundary layer state. Other than that, the differences between the three DDES versions are small. This changes for the positive incidence ($\beta_1 = 138°$). Here, we see much larger differences between DDES results on varying meshes ending with a result almost identical to LES for DDES-fine (see 7-③). We can conclude from Figs. 6 and 7, that the prediction of an accurate transition process is not the most critical part for an accurate prediction of the wake losses. It is the development length of the turbulent boundary layer, i.e. the development of the momentum thickness after the re-attachment, and the boundary layer state at the trailing edge, which has a significant impact on the wake results, also reported by Denton [33]. For $\beta_1 = 128°$, the separation bubble is relatively large and the re-attachment point is close to the trailing edge, hence, there is less space for the turbulent boundary layer to develop. This results in almost identical predictions of the wake losses for all three DDES mesh versions. If the separation bubble becomes shorter and the turbulent boundary layer develops over a longer distance (see Fig. 6, $\beta_1 = 138°$), the accurate prediction of the separation-induced transition and re-attachment points becomes more relevant.

To assess the polar trend prediction with DDES, we show the integral loss coefficient ω_{int} in Fig. 8. This value is determined by area-integrating the loss coefficient ω in pitchwise direction. It is the motivation to use DDES to fill the large gap between RANS and experiment/LES. The previously reported convergence of finer meshes is also seen for ω_{int}. DDES-intermediate shows a very good agreement with experimental reference data whereas

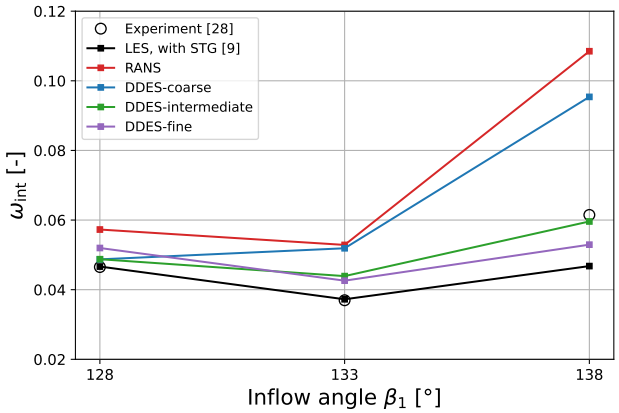

FIGURE 8: Integral total pressure loss coefficient at MP2 (see Fig. 2) for varying inflow angles for Re = 150 000.

DDES-fine tends towards the LES reference. These trends are satisfying, because they confirm the capability of DDES to improve the prediction of the loss polar trend. The deviating results between experiment and LES for the highest inflow angle is also discussed in [9]. Focusing Fig. 7, the loss curve on the right-hand side for $\beta_1 = 138°$ reveals differences between LES and experiment. While the LES results reach zero in the free-stream, the experimental data shows unexpected values different from zero for this specific operating point. This is not seen for other inflow angles. Therefore, it is not possible to say whether the LES

shows a wrong trend or whether the experimental data have some incorrect measurements for this inflow angle.

The above analysis for $Re_1 = 1.5 \times 10^5$ has revealed insights about the predictive capabilities of DDES on different mesh densities. While the coarsest mesh never yields satisfying results, the intermediate and fine resolution showed their potential, but also limitations. DDES results mainly agree well with LES results without an STG at the ADP which helped to explain differences to LES with an STG. The absence of resolved free-stream turbulence is the source of deviations in capturing the separation-induced transition comprehensively. Wissink and Rodi [34] also reported, that the FSTI has a significant impact on the transition length. The growth of Kelvin-Helmholtz instabilities is favored by resolved FSTI. This missing content results in a delayed transition and, hence, a delayed closure of the separation bubble itself. Further, the transition process affects the separation bubble length for this specific low FSTI case, where a longer separated shear layer has a favorable effect on the transition prediction. Moreover, the separation bubble length also affects the wake losses. With the turbulent boundary layer developing over greater lengths, the wake loss predictions do become more sensitive to the mesh resolution which can be linked to the turbulent state of the boundary layer close to the trailing edge.

5. VARIATION OF THE REYNOLDS NUMBER

After having analyzed the DDES for a single Reynolds number, we continue with the comparison of different Reynolds numbers with a specific focus on the off-design operating points ($\beta_1 = 128°$ and $\beta_1 = 138°$). Since no LES exists for higher Reynolds numbers for this test case, yet, we only compare to experimental data in this section.

5.1 Meshing strategy

As part of this study, we aim to provide best possible comparable mesh setups for all Reynolds numbers. Hence, even though the non-dimensional cell sizes are not a suitable measure for a well- or under-resolved mesh (discussed in Sec. 4.1), they normalize cell counts and ensure comparability for different Reynolds numbers by taking flow conditions into account. For this reason, we strive to generate meshes for higher Reynolds numbers based on the resulting non-dimensional cell sizes for $Re_1 = 1.5 \times 10^5$ for every version (coarse, intermediate, fine). Further details about the generation strategy of different mesh densities can be found in Sec. 4.1. The created mesh setups are summarized in Table 3. We generated three meshes each for $Re_1 = 2.5 \times 10^5$ and $Re_1 = 3.5 \times 10^5$. For $Re_1 = 9.0 \times 10^5$, only the coarsest mesh version was considered for two reasons: First, for the highest Reynolds number, RANS already performs quite well, which is why the potential for improvements by DDES is small. Secondly, the total cell count for the coarse mesh is already very large when trying to keep the non-dimensional cell sizes identical to the coarse setups for lower Reynolds numbers. Based on the ratio between the three meshes for other Reynolds numbers, the approximate total cell count for $Re_1 = 9.0 \times 10^5$ for the intermediate or fine mesh resolution would have increased drastically. So we decided not to run such expensive simulations with little potential for improvement compared to the already good RANS results.

TABLE 3: Created mesh setups for varying Reynolds numbers.

	Mesh version	N_{total}	N_{2D}	N_z
Re_1 = 150k	Coarse	66 075	4 405	15
	Intermediate	528 600	17 620	30
	Fine	4 228 800	70 480	60
Re_1 = 250k	Coarse	184 800	8 800	21
	Intermediate	1 901 475	42 255	45
	Fine	12 281 304	146 206	84
Re_1 = 350k	Coarse	598 200	19 940	30
	Intermediate	9 251 124	94 714	66
	Fine	40 488 018	331 869	122
Re_1 = 900k	Coarse	21 662 208	225 648	96

To initially characterize the considered DDES mesh densities for varying Reynolds numbers, we determine the ratio of resolved to total (modeled + resolved) turbulent kinetic energy. This ratio is determined at the re-reattachment location (reported in Tab. 7) for each operating point. The wall-normal boundary layer cut at this location is area-weighted averaged to obtain the percentage of resolved TKE. From Tab. 4, we learn, that for the intermediate and fine mesh, a resolution of at least 90 % is guaranteed, whereas the coarse mesh shows reduced amounts of resolved turbulence. We recall, that no STG was used for these simulations, so the resolved turbulent kinetic energy is only due to the unsteadiness caused by the separated shear layer and turbulent re-attachment. An assessment of this ratio in the wake flow is not useful, because in the wake flow the DDES switches to the resolved branch of the model and differences between all three densities are not that obvious than in the re-attachment region.

5.2 Negative incidence (β_1 = 128°)

We begin with an illustration of the instantaneous 3D flow field with a focus on the blade suction side for all considered meshes and Reynolds numbers for negative incidence in Fig. 9. The separation bubble and the laminar-to-turbulent transition are clearly visible, while the refined meshes yield a better resolution of small-scale turbulent structures for each Reynolds number. In addition, we learn that as the Reynolds number increases, turbulent structures are already well resolved on coarser meshes,

TABLE 4: Ratio of resolved to total turbulent kinetic energy. Values represent the area-weighted average of the wall-normal boundary layer cut at the re-attachment location for each operating point (summarized in Tab. 7).

		$\beta_1 = 128°$	$\beta_1 = 138°$
Re_1 = 150k	Coarse	89.19 %	73.65 %
	Intermediate	96.65 %	96.46 %
	Fine	97.55 %	97.59 %
Re_1 = 250k	Coarse	90.51 %	81.68 %
	Intermediate	97.09 %	93.83 %
	Fine	97.41 %	97.20 %
Re_1 = 350k	Coarse	89.75 %	81.67 %
	Intermediate	96.62 %	97.62 %
	Fine	96.74 %	96.86 %
Re_1 = 900k	Coarse	91.06 %	94.03 %

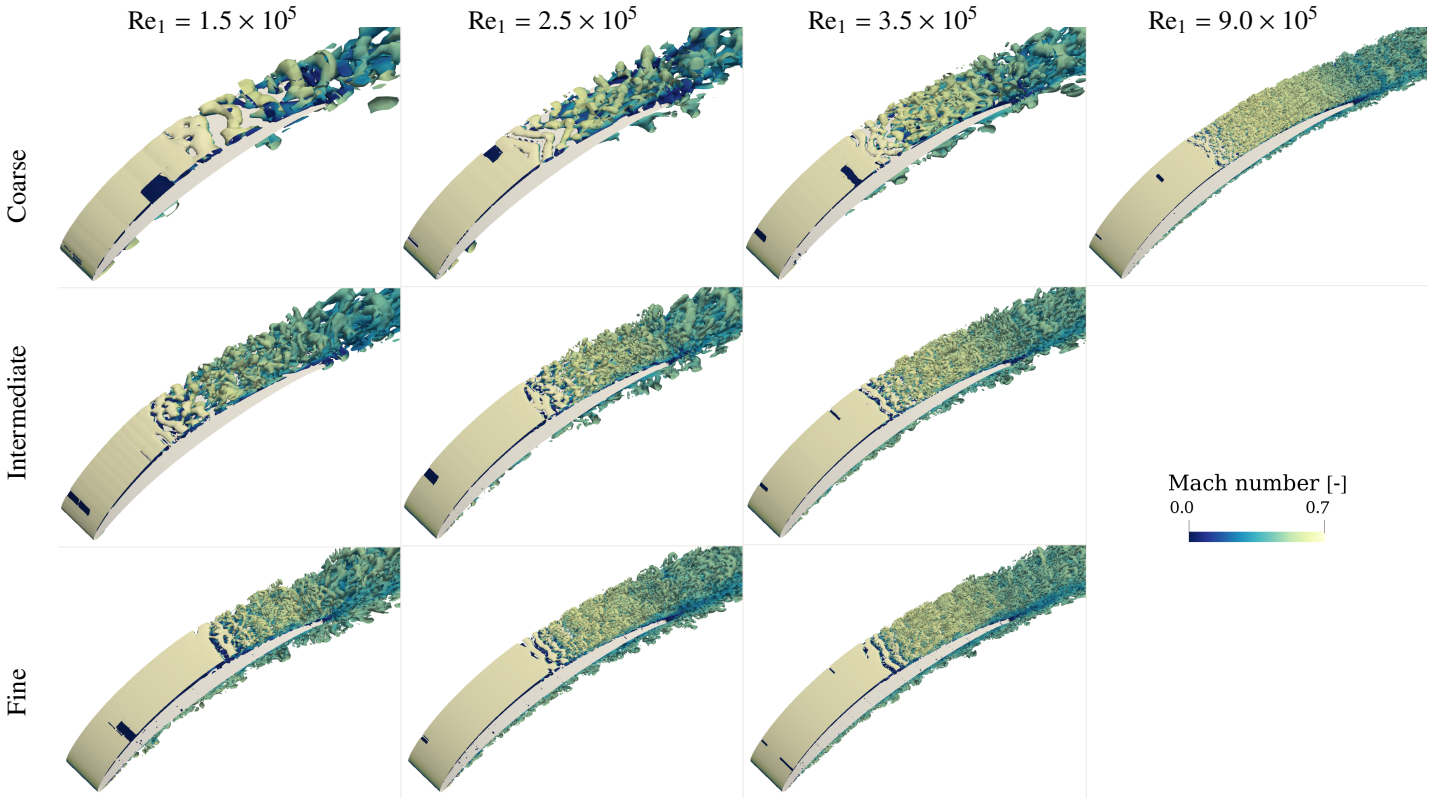

FIGURE 9: Illustration of the instantaneous 3D flow field through the Q-criterion colored by the Mach number with a focus on the blade suction side for negative incidence.

while the non-dimensional cell sizes are comparable to those at lower Reynolds numbers. The shift in the onset of separation and transition is already visible in the resolved scales and will be discussed in the following.

The inflow Mach number (see Tab. 1) is kept constant for all operating points which is confirmed by the M_{is} results (not shown here). Hence, the increasing Reynolds number was achieved by a change in the kinematic viscosity ν, which effectively results in a change in the fluid density and affects the boundary layer. This can be seen by looking at the C_f values in Fig. 10. The global trend of a shrinking separation bubble with increasing Reynolds numbers can be observed on both the suction and pressure side (also reported in [35]). Focusing on the pressure side (dashed lines) the differences between all simulations decrease for increasing Reynolds number. The above-mentioned oscillating result by RANS at the leading edge separation for $Re_1 = 1.5 \times 10^5$ is stabilized with increasing Reynolds numbers. Further, RANS and the DDES mesh versions converge and nearly collapse for $Re_1 = 9.0 \times 10^5$ on the pressure side (see 10-①). Results on the suction side (solid lines) reveal twofold trends. For $Re_1 = 2.5 \times 10^5$ and $Re_1 = 3.5 \times 10^5$, RANS and DDES-coarse show comparable results for the transition onset whereas DDES-intermediate and DDES-fine also agree well with each other, but with a transition onset further downstream (see 10-②). Generally, the differences between RANS and all DDES mesh versions become smaller with increasing Reynolds number. As discussed in Sec. 4, the missing resolved turbulence becomes more relevant to correctly 'close' the separation bubble for the negative incidence and separation bubbles are consistently predicted larger in comparison to the RANS results.

The effect of the Reynolds number on predicted wake total pressure loss coefficient is shown in Fig. 11. For the negative incidence, the RANS results show improving agreement with the experiment for increasing Reynolds numbers. On the other hand, trends from Fig. 10 for the three DDES versions can also be found here. While DDES-coarse is inaccurate for $Re_1 = 1.5 \times 10^5$, the DDES results converge with increasing Reynolds number. Overall, a very good agreement of the wake losses is realized with DDES-intermediate and DDES-fine. For $Re_1 = 9.0 \times 10^5$ we see deviations for DDES-coarse that end up in an underestimation of the wake losses.

To facilitate understanding of the trends for increasing Reynolds numbers, we illustrate the separation bubble shape for DDES simulations in Fig. 12. The lines represent the shear layer border $u_{tang}/u_{mag,1,int} = 0$, dividing the flow field in forward and reversed flow, where u_{tang} is the velocity component tangential to the blade surface. With increasing Reynolds number, the separation bubble not only shrinks in streamwise, but also in wall-normal direction η. A reduced height of the separation bubble yields a reduced intensity of the separated flow which is also seen by less negative C_f values in the separated region in Fig. 10. The reduced separation bubble size and intensity is directly linked to the resolved turbulence predicted by DDES. Further details of the separation bubble characteristics are summarized in Appendix B.

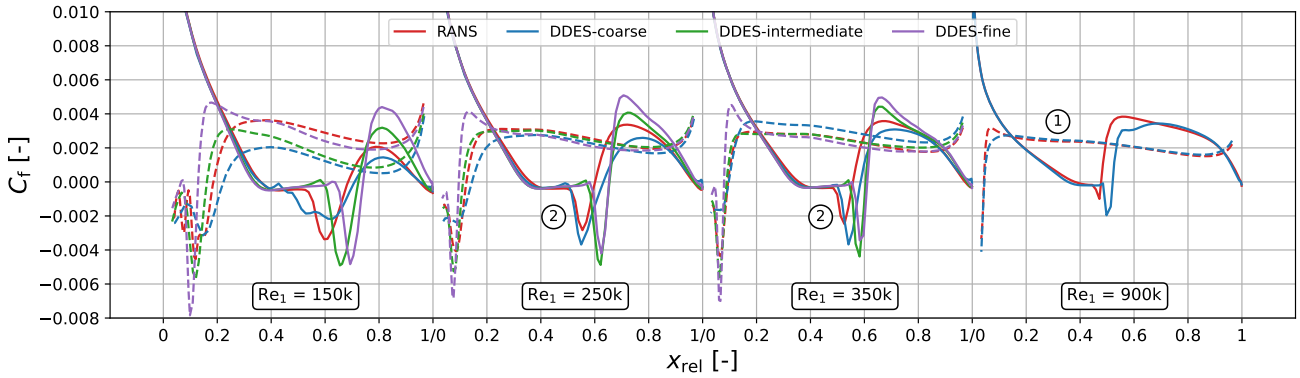

FIGURE 10: Skin friction coefficient along the blade suction (—) and pressure (- -) side for varying Reynolds numbers for negative incidence.

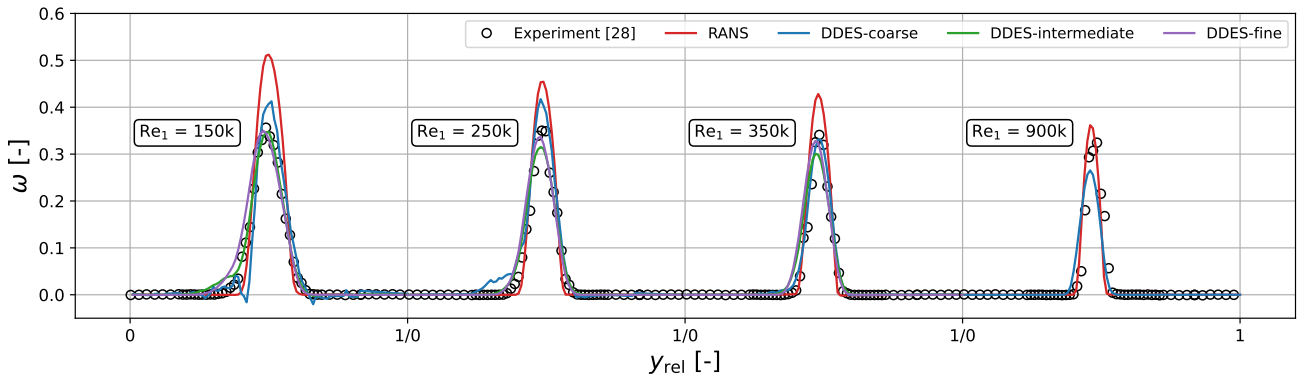

FIGURE 11: Total pressure loss coefficient at MP2 (see Fig. 2) for varying Reynolds numbers for negative incidence.

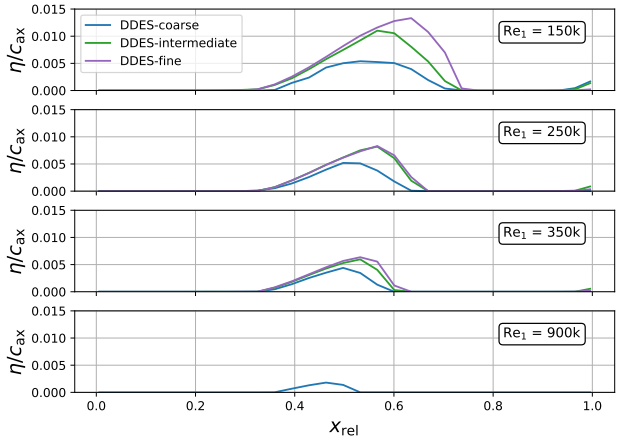

FIGURE 12: Separation bubble shape illustrated by the shear layer border ($u_{tang}/u_{mag,1,int} = 0$) for varying Reynolds numbers for negative incidence.

Figure 13 depicts the wall-normal boundary layer cuts of the resolved turbulent kinetic energy k_{res} after the re-attachment (probe locations are illustrated in Fig. 2) for varying Reynolds numbers and mesh densities. Results for the three mesh versions collapse with increasing Reynolds numbers, but most importantly, the overall level of resolved TKE decreases for higher Reynolds numbers. Hence, improved results by the DDES cannot be expected for smaller separation bubbles at higher Reynolds numbers, because there is no resolved content present, basically produced by larger separation regimes. Additionally, the model reduces modeled turbulence (as intended by the model in separated regions) to a minimum which yields modeled stress depletion [15, 36]. This is the case especially for DDES-coarse at $Re_1 = 9.0 \times 10^5$.

Finally, Fig. 14 shows an improved prediction of the trend in area-integrated loss coefficient for the intermediate and fine mesh version compared to RANS results. DDES-coarse yields varying results for $Re_1 = 1.5 \times 10^5$ up to $Re_1 = 3.5 \times 10^5$ ending in a fairly good agreement with experimental data at $Re_1 = 9.0 \times 10^5$. This integrated value for DDES-coarse has to be assessed with caution, because the agreement looks good compared to the experiment, but the qualitatively trend shown in Fig. 11 reveals differences.

5.3 Positive incidence ($\beta_1 = 138°$)

For the positive incidence ($\beta_1 = 138°$), DDES performs differently. An assessment of the isentropic Mach number in Fig. 15 emphasizes, that the deviations between all three DDES meshes are marginal in terms of the blade pressure distribution, except for $Re_1 = 1.5 \times 10^5$ which has been discussed in Sec. 4.3. Further, significant differences between RANS and DDES are not noticeable for higher Reynolds numbers. The results are in good agreement with the experiment except for the exact shape of the separation bubble.

In Fig. 16 we show results for the pressure loss coefficient

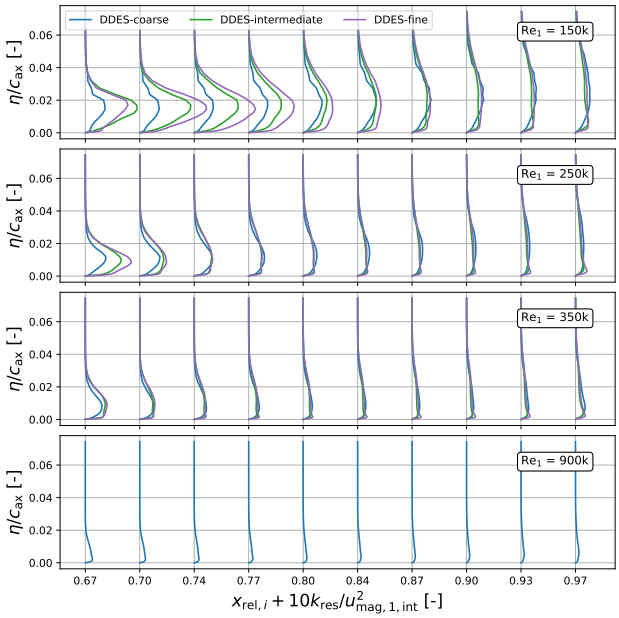

FIGURE 13: Wall-normal boundary layer cuts of the resolved turbulent kinetic energy on the blade suction side after re-attachment (probe locations illustrated in Fig. 2) for varying Reynolds number for negative incidence.

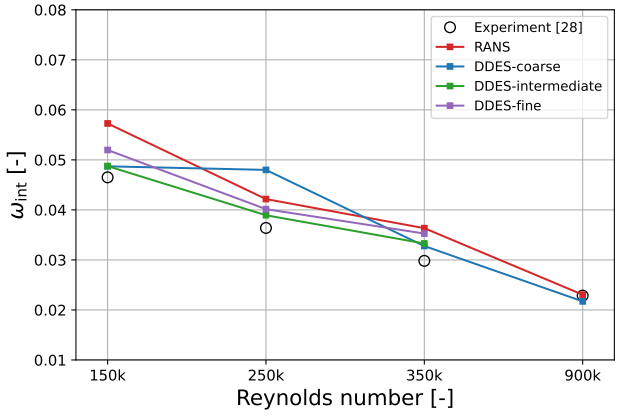

FIGURE 14: Integral total pressure loss coefficient at MP2 (see Fig. 2) for varying Reynolds numbers for negative incidence.

in the wake at MP2. RANS tends towards the experimental data with increasing Reynolds number and does a good job in predicting the maximum peak value of the loss coefficient. Even the wake shape is predicted with good agreement, except for $Re_1 = 9.0 \times 10^5$ where we see a pitchwise shift and a too narrow wake width prediction of the RANS results. The DDES results reveal a negative trend for increasing Reynolds numbers and positive incidence. A constant drift away from experimental reference data is visible with growing discrepancies for higher Reynolds numbers. This is also seen for the integral loss coefficient in Fig. 17.

This negative trend can be explained with the increasing development length of the turbulent boundary layer along the blade surface after the re-attachment. Since the separation bubble occurs close to the leading edge and shrinks with increasing Reynolds number, the interaction of modeled and resolved scales to appropriately capture the boundary layer development is essential for these operating points. Boundary layer cuts of the modeled TKE, shown in Fig. 18, reveal a noticeable reduction for increasing Reynolds numbers. However, the smaller separation bubble has the effect that resolved turbulence is not generated as required, leading to modeled stress depletion in attached boundary layer again. This ends in a poor representation of the turbulent boundary layer close to the trailing edge which affects the wake flow prediction.

The variation of the Reynolds number revealed multiple aspects about the capabilities and limitations of DDES. For the negative incidence, DDES performs good and agrees well with the experiments. With increasing Reynolds number, the benefit of a finer mesh resolution diminishes. It was found that the boundary layer state on the blade suction side mainly determines the wake flow. The positive incidence results emphasize limitations of the DDES setup without STG. The missing resolved turbulence in combination with a relatively small separation bubble and long development lengths of the turbulent boundary layer after re-attachment are key factors for deviating DDES results. This becomes more prominent with increasing Reynolds number.

5.4 Discussion of computational costs

The computational results obtained, with varying degrees of accuracy, can be put into perspective considering the computational costs of the DDES method. We summarized the simulation duration in Tab. 5. To ensure comparability with LES, different mesh resolutions (resulting in different block splitting) and along all Reynolds numbers, we report the required central processing unit (CPU) hours (referring to a single core) for one convective through flow. For all DDES simulations, these are the arithmetic means of the cost for $\beta_1 = 128°$ and $\beta_1 = 138°$. It can be stated that DDES-intermediate is considerably cheaper by a factor of 20 than LES at the lowest Reynolds number of $Re_1 = 1.5 \times 10^5$. Recalling the motivation for the DDES method as being more accurate than RANS but cheaper than LES, we find that to be the case for $Re_1 = 1.5 \times 10^5$. Nevertheless, LES introduces less modeling uncertainty and cannot be replaced by DDES as numerical references. The rapidly increasing computational costs for higher Reynolds numbers can be seen as problematic. While we have seen improved results for the negative incidence, the predictive

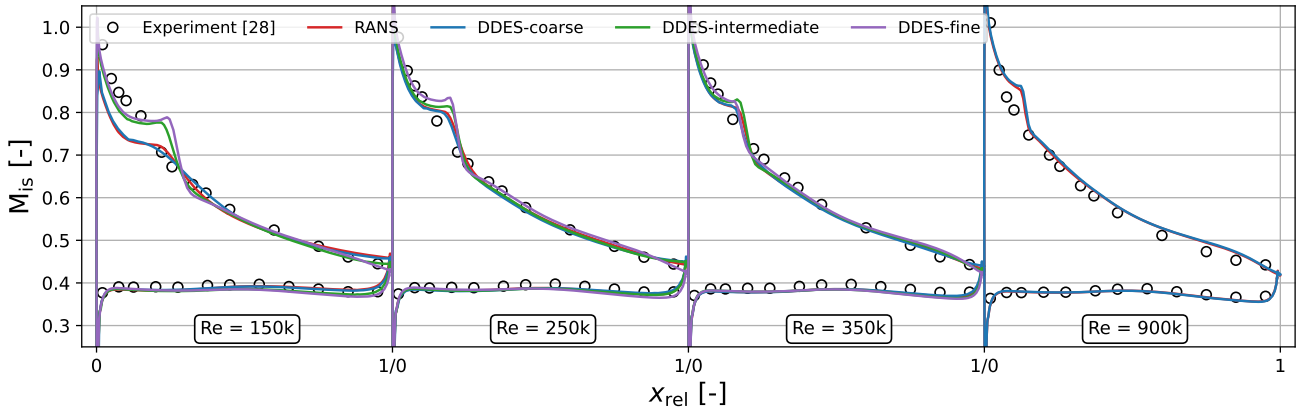

FIGURE 15: Isentropic Mach number along the blade surface for varying Reynolds numbers for positive incidence.

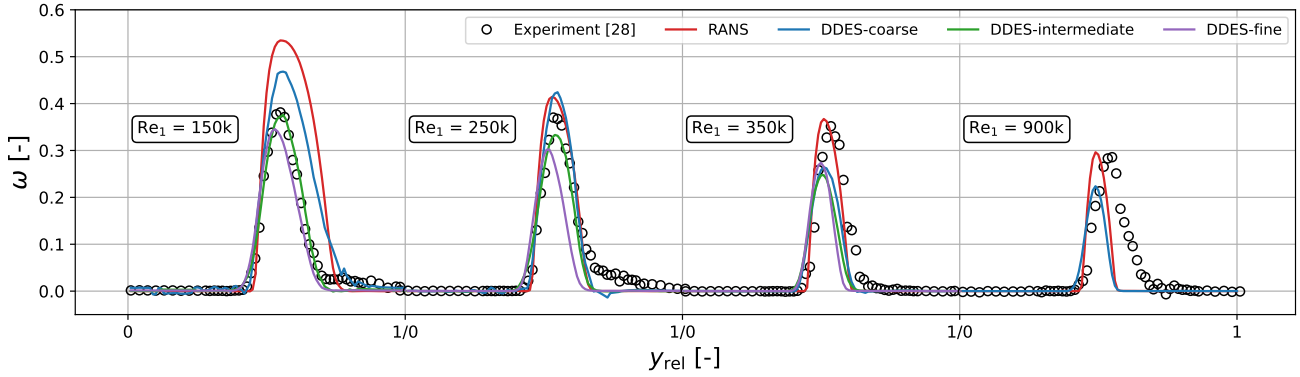

FIGURE 16: Total pressure loss coefficient at MP2 (see Fig. 2) for varying Reynolds numbers for positive incidence.

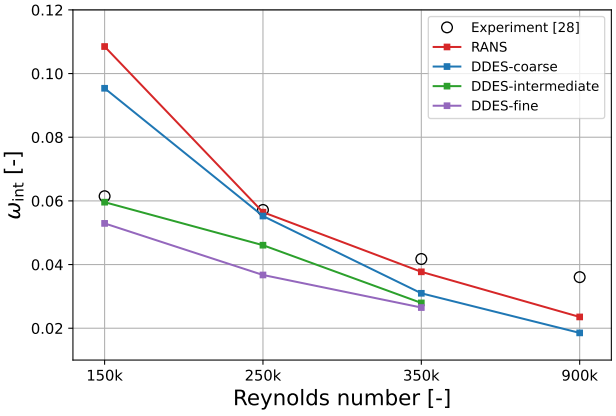

FIGURE 17: Integral total pressure loss coefficient at MP2 (see Fig. 2) for varying Reynolds numbers for positive incidence.

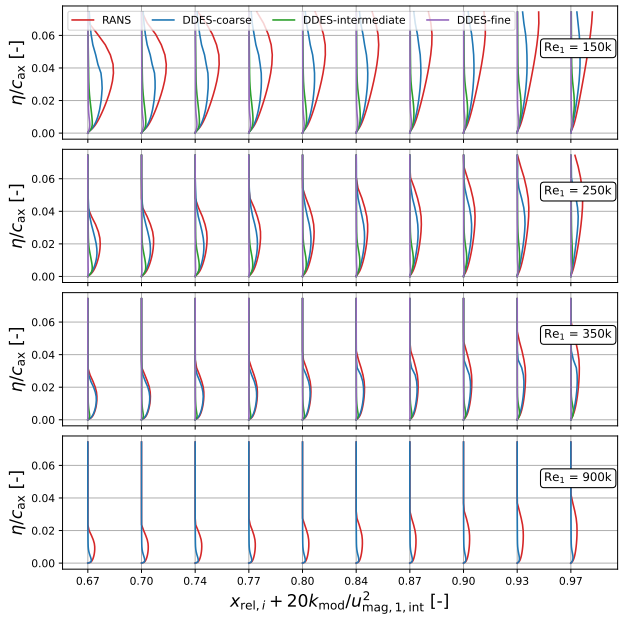

FIGURE 18: Wall-normal boundary layer cuts of the modeled turbulent kinetic energy on the blade suction side after re-attachment (probe locations illustrated in Fig. 2) for positive incidence.

TABLE 5: Simulation duration (in hours) per convective through flow on a single CPU. Durations for RANS simulations were recorded until numerical convergence of the residual norm.

		Re_1 = 150k	Re_1 = 250k	Re_1 = 350k	Re_1 = 900k
LES		4 816.8	*n.a.*	*n.a.*	*n.a.*
DDES	Coarse	40.0	89.1	281.9	21 219.5
	Intermediate	236.7	770.4	3 512.6	*n.a.*
	Fine	2 404.5	10 085.9	48 052.4	*n.a.*
RANS	Fine	5.0	11.5	19.7	23.8

quality for the positive incidence did not improve, on the contrary, it showed a trend drifting away from experiments. Therefore, the benefit of such an expensive simulation, with respect to RANS, can be considered questionable for $\beta_1 = 138°$.

6. CONCLUSIONS

With this study, we provide a thorough assessment of the transitional DDES model and its performance for the prediction of a transitional compressor cascade flow with relevant phenomena such as laminar-to-turbulent transition, separation and turbulent wakes. To account for different operating conditions, we varied Reynolds numbers and inflow angles. We also considered three mesh densities for DDES to assess the resolution requirements for changing operating conditions. Initially, we validated the predictive quality of DDES by comparison with LES and experimental reference data for the lowest Reynolds number ($Re_1 = 1.5 \times 10^5$). This was done by evaluating relevant operating points in design and off-design conditions through a variation of inflow angle. Finally, we analyzed the effect of varying Reynolds number for both off-design inflow angles. With respect to the research questions formulated above, our study has yielded the following results:

- For the lowest Reynolds number, DDES is capable of predicting the relevant flow physics with improved quality compared to RANS when using a sufficient mesh resolution. The coarsest DDES mesh setup failed to capture the relevant mechanisms, which emphasizes, that at least the reported intermediate mesh resolution is required to account for the growing instabilities in the separated shear layer.

- All DDES simulations were conducted without a synthetic turbulence generator. The comparison with an LES that was also carried out without an STG revealed a convergence of the DDES towards the LES with refined meshes (still much coarser than the LES mesh count). This comparison and the visible differences to an LES with STG helped to classify the numerical behavior of the DDES method.

- The Reynolds number variation for negative incidence ($\beta_1 = 128°$) demonstrated the potential of the DDES method. The connection between the boundary layer development and wake losses has been evaluated and revealed a strong interaction between the separation bubble size itself, the associated production of modeled and resolved turbulence and the resulting wake losses. DDES gives consistently good agreement in the wake region, confirmed by the Reynolds number lapse rate of the integral loss coefficient. Generally, the intermediate mesh setup was already capable of predicting the flow field accurately enough. Deviations for the highest Reynolds number have been explained by the presence of the smallest separation bubble size, which suffers the most from modeled stress depletion.

- The Reynolds number variation for the positive incidence ($\beta_1 = 138°$) revealed limitations of the investigated DDES setup. Observed deviations from the experiments could be explained with the interaction of reduced modeled turbulent kinetic energy and missing resolved inflow turbulence. This specific operating condition, characterized by a small separation bubble and large development length along the blade surface, misses turbulence which is required to capture the correct turbulent boundary layer state. A clear recommendation concerning the mesh resolution cannot be made based on the results for this specific inflow angle.

In terms of computational cost, DDES shows a saving potential compared to LES while it is significantly more expensive than RANS. The decision as to whether the DDES method is appropriate for a particular problem depends on the expectations of the CFD practitioner.

This study is a comprehensive examination of the transitional DDES method highlighting the capabilities and potential of this approach for the application to a wide operating range. At the same time, it identifies conceptual limitations and calls for further exploration of the method. Missing resolved turbulence appears to be a key factor in the deviation of DDES results from reference data for some operating points. A logical next step is the introduction of an STG for the intermediate and fine meshes, which might improve the representation of laminar-to-turbulent transition and the developing turbulent boundary layers. In this respect, it would also be interesting to investigate the introduction of resolved turbulence only in the separated shear layer, based on information from the underlying transition model.

ACKNOWLEDGEMENTS

The authors gratefully acknowledge the scientific support and HPC resources provided by the German Aerospace Center (DLR). All simulations in this work have been carried out on the HPC system CARA[2] which is partially funded by 'Saxon State Ministry for Economic Affairs, Labour and Transport' and 'Federal Ministry for Economic Affairs and Climate Action'. Other than that, this research did not receive any specific grant from funding agencies in the public, commercial, or non-for-profit sectors.

[2] https://www.top500.org/system/179779

REFERENCES

[1] Denton, John D. "Some Limitations of Turbomachinery CFD." *Volume 7: Turbomachinery, Parts A, B, and C*: pp. 735–745. 2010. ASMEDC. DOI 10.1115/gt2010-22540.

[2] Montomoli, Francesco, Carnevale, Mauro, D'Ammaro, Antonio, Massini, Michela and Salvadori, Simone. *Limitations in Turbomachinery CFD*. Springer International Publishing (2015): pp. 21–32. DOI 10.1007/978-3-319-14681-2_2.

[3] Tyacke, James, Vadlamani, N.R., Trojak, W., Watson, R., Ma, Y. and Tucker, P.G. "Turbomachinery simulation challenges and the future." *Progress in Aerospace Sciences* Vol. 110 (2019): p. 100554. DOI 10.1016/j.paerosci.2019.100554.

[4] Bergmann, Michael, Morsbach, Christian, Klose, Bjoern F., Ashcroft, Graham and Kügeler, Edmund. "A Numerical Test Rig for Turbomachinery Flows Based on Large Eddy Simulations With a High-Order Discontinuous Galerkin Scheme—Part I: Sliding Interfaces and Unsteady Row Interactions." *Journal of Turbomachinery* Vol. 146 No. 2 (2023): p. 021005. DOI 10.1115/1.4063734.

[5] Klose, Bjoern F., Morsbach, Christian, Bergmann, Michael, Hergt, Alexander, Klinner, Joachim, Grund, Sebastian and Kügeler, Edmund. "A Numerical Test Rig for Turbomachinery Flows Based on Large Eddy Simulations With a High-Order Discontinuous Galerkin Scheme—Part II: Shock Capturing and Transonic Flows." *Journal of Turbomachinery* Vol. 146 No. 2 (2023): p. 021006. DOI 10.1115/1.4063827.

[6] Morsbach, Christian, Bergmann, Michael, Tosun, Adem, Klose, Bjoern F., Bechlars, Patrick and Kügeler, Edmund. "A Numerical Test Rig for Turbomachinery Flows Based on Large Eddy Simulations With a High-Order Discontinuous Galerkin Scheme—Part III: Secondary Flow Effects." *Journal of Turbomachinery* Vol. 146 No. 2 (2023): p. 021007. DOI 10.1115/1.4063511.

[7] Sandberg, Richard D. and Michelassi, Vittorio. "The Current State of High-Fidelity Simulations for Main Gas Path Turbomachinery Components and Their Industrial Impact." *Flow, Turbulence and Combustion* Vol. 102 No. 4 (2019): pp. 797–848. DOI 10.1007/s10494-019-00013-3.

[8] Yao, Jie and Teo, C. J. "A Mesh Size Scaling Law with Reynolds Number for Large Eddy Simulation in Channel Flow." *Advances in Applied Mathematics and Mechanics* Vol. 14 No. 6 (2022): pp. 1535–1566. DOI 10.4208/aamm.oa-2021-0296.

[9] Bergmann, Michael, Morsbach, Christian, Möller, Felix M., Klose, Bjoern F., Hergt, Alexander and Goinis, Georgios. "A comparative study of varying incidence angle effects on a low-Reynolds-number compressor cascade based on experiments, low-fidelity and high-fidelity numerical simulations." *16th European Conference on Turbomachinery Fluid Dynamics and Theromdynamics*: p. 231. 2025. European Turbomachinery Society.

[10] Pacciani, Roberto, Marconcini, Michele, Arnone, Andrea and Bertini, Francesco. "Predicting High-Lift Low-Pressure Turbine Cascades Flow Using Transition-Sensitive Turbulence Closures." *Journal of Turbomachinery* Vol. 136 No. 5 (2013): p. 051007. DOI 10.1115/1.4025224.

[11] Mansour, Mahmoud L., Konan, S. Murthy and Goswami, Shraman. "Prediction of Lapse Rate in Low Pressure Turbines With and Without Modeling of the Laminar-Turbulent Transition." *Volume 6: Turbo Expo 2007, Parts A and B*: pp. 1189–1197. 2007. ASME. DOI 10.1115/gt2007-27110.

[12] Mays, Michael D., Lardeau, Sylvain and Laizet, Sylvain. "Capturing the drag crisis in the flow around a smooth cylinder using a hybrid RANS-LES model on coarse meshes." *International Journal of Heat and Fluid Flow* Vol. 103 (2023): p. 109203. DOI 10.1016/j.ijheatfluidflow.2023.109203.

[13] Zhou, Lin, Gao, Zhenghong and Du, Yiming. "Flow-dependent DDES/γ-$\mathrm{Re}_{\theta t}$ coupling model for the simulation of separated transitional flow." *Aerospace Science and Technology* Vol. 87 (2019): pp. 389–403. DOI 10.1016/j.ast.2019.02.037.

[14] Tucker, P.G. *Unsteady Computational Fluid Dynamics in Aeronautics*. Springer Netherlands (2014). DOI 10.1007/978-94-007-7049-2.

[15] Spalart, P. R., Deck, S., Shur, M. L., Squires, K. D., Strelets, M. Kh. and Travin, A. "A New Version of Detached-eddy Simulation, Resistant to Ambiguous Grid Densities." *Theoretical and Computational Fluid Dynamics* Vol. 20 No. 3 (2006): pp. 181–195. DOI 10.1007/s00162-006-0015-0.

[16] Menter, F. R. "Two-equation eddy-viscosity turbulence models for engineering applications." *AIAA Journal* Vol. 32 No. 8 (1994): pp. 1598–1605. DOI 10.2514/3.12149.

[17] Spalart, P.R., Jou, W.-H., Strelets, M. and Allmaras, S.R. "Comments on the feasability of LES for wings, and on a hybrid RANS/LES approach." *Computer Science* (1997): pp. 1–11.

[18] Shur, Mikhail L., Spalart, Philippe R., Strelets, Mikhail Kh. and Travin, Andrey K. "An Enhanced Version of DES with Rapid Transition from RANS to LES in Separated Flows." *Flow, Turbulence and Combustion* Vol. 95 No. 4 (2015): pp. 709–737. DOI 10.1007/s10494-015-9618-0.

[19] Möller, Felix M., Tucker, Paul G., Wang, Zhong-Nan, Morsbach, Christian and Bergmann, Michael. "On the Prediction of Separation-Induced Transition by Coupling Delayed Detached-Eddy Simulation with γ-Transition Model." *15th European Conference on Turbomachinery Fluid Dynamics and Thermodynamics*: p. 375. 2023. European Turbomachinery Society. DOI 10.29008/etc2023-375.

[20] Möller, Felix M., Tucker, Paul G., Wang, Zhong-Nan and Morsbach, Christian. "Transitional Delayed Detached-Eddy Simulation for a Compressor Cascade: A Critical Assessment." *Journal of Propulsion and Power* Vol. 40 No. 4 (2024): pp. 533–546. DOI 10.2514/1.b39344.

[21] Menter, Florian R., Smirnov, Pavel E., Liu, Tao and Avancha, Ravikanth. "A One-Equation Local Correlation-Based Transition Model." *Flow, Turbulence and Combustion* Vol. 95 No. 4 (2015): pp. 583–619. DOI 10.1007/s10494-015-9622-4.

[22] Geiser, Georg, Wellner, Jens, Kügeler, Edmund, Weber, Anton and Moors, Anselm. "On the Simulation and Spec-

tral Analysis of Unsteady Turbulence and Transition Effects in a Multistage Low Pressure Turbine." *Journal of Turbomachinery* Vol. 141 No. 5 (2019): p. 051012. DOI 10.1115/1.4041820.

[23] Shu, Chi-Wang and Osher, Stanley. "Efficient implementation of essentially non-oscillatory shock-capturing schemes." *Journal of Computational Physics* Vol. 77 No. 2 (1988): pp. 439–471. DOI 10.1016/0021-9991(88)90177-5.

[24] Travin, A., Shur, M., Strelets, M. and Spalart, P. R. "Physical and Numerical Upgrades in the Detached-Eddy Simulation of Complex Turbulent Flows." *Fluid Mechanics and Its Applications: Advances in LES of Complex Flows*. Springer Netherlands (2002): pp. 239–254. DOI 10.1007/0-306-48383-1_16.

[25] Roe, P.L. "Approximate Riemann solvers, parameter vectors, and difference schemes." *Journal of Computational Physics* Vol. 43 No. 2 (1981): pp. 357–372. DOI 10.1016/0021-9991(81)90128-5.

[26] Strelets, M. "Detached eddy simulation of massively separated flows." *39th Aerospace Sciences Meeting and Exhibit*: p. 879. 2001. American Institute of Aeronautics and Astronautics. DOI 10.2514/6.2001-879.

[27] Kato, M. and Launder, B.E. "The modeling of turbulent flow around stationary and vibrating square cylinders." *9th Symposium on Turbulent Shear Flows*: pp. 10.4.1–10.4.6. 1993.

[28] Hergt, A., Pesch, M., Grund, S. and Flamm, J. "Low Reynolds Number Effects in Compressor Blade Design." *International Journal of Gas Turbine, Propulsion and Power Systems* Vol. 15 No. 4 (2024): p. v15n4tp08. DOI 10.38036/jgpp.15.4_v15n4tp08.

[29] Giles, Michael. "UNSFLO: A Numerical Method For The Calculation Of Unsteady Flow In Turbomachinery." *Technical Report, Gas Turbine Laboratory*: pp. 1–91. 1991.

[30] Bolinches-Gisbert, M., Robles, David Cadrecha, Corral, Roque and Gisbert, Fernando. "Prediction of Reynolds Number Effects on Low-Pressure Turbines Using a High-Order ILES Method." *Journal of Turbomachinery* Vol. 142 No. 3 (2020): p. 031002. DOI 10.1115/1.4045776.

[31] Bergmann, Michael, Morsbach, Christian, Ashcroft, Graham and Kügeler, Edmund. "Statistical Error Estimation Methods for Engineering-Relevant Quantities From Scale-Resolving Simulations." *Journal of Turbomachinery* Vol. 144 No. 3 (2021): p. 031005. DOI 10.1115/1.4052402.

[32] Celik, Ismail B., Ghia, Urmila, Roache, Patrick J., Freitas, Christopher J., Coleman, Hugh and Raad, Peter E. "Procedure for Estimation and Reporting of Uncertainty Due to Discretization in CFD Applications." *Journal of Fluids Engineering* Vol. 130 No. 7 (2008): p. 078001. DOI 10.1115/1.2960953.

[33] Denton, J. D. "Loss Mechanisms in Turbomachines." *Volume 2: Combustion and Fuels; Oil and Gas Applications; Cycle Innovations; Heat Transfer; Electric Power; Industrial and Cogeneration; Ceramics; Structures and Dynamics; Controls, Diagnostics and Instrumentation; IGTI Scholar Award*: p. 435. 1993. American Society of Mechanical Engineers. DOI 10.1115/93-gt-435.

[34] Wissink, J. G. and Rodi, W. "Direct Numerical Simulations of Transitional Flow in Turbomachinery." *Journal of Turbomachinery* Vol. 128 No. 4 (2006): pp. 668–678. DOI 10.1115/1.2218517.

[35] Volino, Ralph J. "Separated Flow Transition Under Simulated Low-Pressure Turbine Airfoil Conditions—Part 1: Mean Flow and Turbulence Statistics." *Journal of Turbomachinery* Vol. 124 No. 4 (2002): pp. 645–655. DOI 10.1115/1.1506938.

[36] Ashton, Neil. "Recalibrating Delayed Detached-Eddy Simulation to eliminate modelled-stress depletion." *23rd AIAA Computational Fluid Dynamics Conference*: pp. 1962–1975. 2017. American Institute of Aeronautics and Astronautics. DOI 10.2514/6.2017-4281.

APPENDIX A. DETAILED MESH INFORMATION

Table 6 gives a comprehensive summary of all relevant mesh properties for the investigated DDES setups. The Δy^+ value represents the wall-normal cell length and not the first distance to the cell center which is typically referred to as y^+. Hence, in Tab. 6, the recommended threshold value is $\Delta y^+ \leq 2$, whereas values ≤ 3 are also acceptable. The non-dimensional cell sizes are given as ranges because the flow field changes for positive and negative incidence. The range indicates maximum values on the suction and pressure side for each variable. To eliminate the impact of leading and trailing edge effects on the extracted values, we only consider the non-dimensional cell sizes for $0.05 \leq x_{\mathrm{rel}} \leq 0.95$. $\mathrm{N}_{i,\mathrm{SS}}$ and $\mathrm{N}_{i,\mathrm{PS}}$ are the streamwise resolution on the blade suction and pressure side, respectively. $\mathrm{N}_{j,\mathrm{sep}}$ is the number of cells in wall-normal direction inside the separation bubble. Ranges are given because the separation bubble shape changes for positive and negative incidence.

APPENDIX B. SEPARATION BUBBLE CHARACTERISTICS

Table 7 summarizes the characteristics of the primary separation bubble on the blade suction side for all conducted DDES simulations. The separation onset remains almost identical for all Reynolds numbers for a given incidence angle. Only the separation bubble size changes, both in length and height. This is also reported in the literature [35]. The separation bubble height η_{sep} is defined by the maximum wall-normal distance η along the shear layer border $u_{\mathrm{tang}}/u_{\mathrm{mag},1,\mathrm{int}} = 0$, dividing reversed and forward flow. An illustration of the separation bubble shape is also given in Fig. 12 as an example for the negative incidence.

TABLE 6: Comprehensive summary of created mesh setups.

	Mesh version	N_{total}	N_{2D}	N_z	Δx^+	Δy^+	Δz^+	$N_{i,SS}$	$N_{i,PS}$	$N_{j,sep}$
	Coarse	66 075	4 405	15	155 – 206	2 – 3	92 – 144	78	67	6 – 9
Re_1 = 150k	Intermediate	528 600	17 620	30	81 – 107	2 – 3	49 – 74	156	134	12 – 15
	Fine	4 228 800	70 480	60	42 – 54	2 – 3	26 – 37	312	268	23 – 26
	Coarse	184 800	8 800	21	162 – 224	2 – 3	96 – 147	108	93	8 – 10
Re_1 = 250k	Intermediate	1 901 475	42 255	45	79 – 101	2 – 3	51 – 70	234	201	19 – 20
	Fine	12 281 304	146 206	84	43 – 54	2 – 3	28 – 37	436	374	27 – 33
	Coarse	598 200	19 940	30	158 – 187	2 – 3	94 – 130	156	134	11 – 16
Re_1 = 350k	Intermediate	9 251 124	94 714	66	74 – 87	1 – 2	46 – 59	342	294	28 – 31
	Fine	40 488 018	331 869	122	40 – 54	1 – 2	24 – 32	638	547	33 – 41
Re_1 = 900k	Coarse	21 662 208	225 648	96	105 – 131	1 – 2	64 – 89	498	428	24 – 34

TABLE 7: Separation bubble characteristics for all simulations.

		$\beta_1 = 128°$				$\beta_1 = 138°$			
		$x_{rel,sep,onset}$	$x_{rel,sep,end}$	$l_{rel,sep}$	η_{sep}/c_{ax}	$x_{rel,sep,onset}$	$x_{rel,sep,end}$	$l_{rel,sep}$	η_{sep}/c_{ax}
	Coarse	0.360	0.706	0.347	0.00539	0.055	0.545	0.490	0.00708
Re_1 = 150k	Intermediate	0.338	0.718	0.380	0.01102	0.068	0.304	0.237	0.00620
	Fine	0.328	0.732	0.405	0.01333	0.066	0.294	0.228	0.00751
	Coarse	0.345	0.620	0.275	0.00520	0.053	0.248	0.194	0.00362
Re_1 = 250k	Intermediate	0.331	0.654	0.322	0.00820	0.061	0.246	0.186	0.00408
	Fine	0.328	0.653	0.325	0.00846	0.056	0.225	0.169	0.00400
	Coarse	0.338	0.582	0.244	0.00439	0.051	0.203	0.151	0.00236
Re_1 = 350k	Intermediate	0.330	0.597	0.267	0.00596	0.056	0.214	0.158	0.00311
	Fine	0.330	0.597	0.267	0.00641	0.071	0.195	0.124	0.00181
Re_1 = 900k	Coarse	0.352	0.514	0.161	0.00180	0.051	0.149	0.098	0.00098